ROYAL SOCIETY
OF CHEMISTRY

PAPER

Check for updates

Rationale, design and initial performance of a dual-wavelength (157 & 193 nm) cryo-LA-ICP-MS/MS system

Tobias Erhardt, [ID] *ab C. Ashley Norris, [ID] c Ruben Rittberger, ab Michael Shelley, d Martin Kutzschbach, [ID] ab Linda Marko, ab Alexander Schmidt ab and Wolfgang Müller [ID] *ab

Owing to their wide applicability and relative ease of use, 193 nm ArF excimer lasers are commonly-used laser sources for laser ablation inductively-coupled plasma mass spectrometry (LA-ICP-MS). However, some materials, like quartz, sulphates, potassium salts, fused silica or water ice, often show poor ablation characteristics at 193 nm due to low absorption at deep-UV (DUV) wavelengths. Only very few LA-ICP-MS systems have utilized 157 nm F_2 excimer lasers, likely due to their low laser energy output in combination with the challenges that the transmission of vacuum-UV (VUV) radiation poses. Nevertheless, by using a 157 nm laser, some of the shortcomings of 193 nm LA can be overcome, because many of the "difficult to ablate" materials are opaque at 157 nm and the ~20% higher photon energies at 157 nm. Here we describe a custom-built dual-wavelength (157 nm & 193 nm) cryo-LA-ICP-MS/MS system, built around the RESOlution-SE LA system with an S155 two-volume ablation cell, to which a separate 157 nm beam path was added. The system utilizes two distinct laser sources and beam paths for the two wavelengths, each optimized for the specific requirements and use-cases, and facilitates switching between the wavelengths within less than half a day. Furthermore, the system can be equipped with a newly-designed large cryo-sample holder for the S155 LA cell to analyze natural ice samples. Alongside the characterization of the 157 nm beam path, yielding on-sample fluences of up to 8 J cm^{-2}, we present comparative results of ablation characteristics for a range of materials at the two wavelengths, including threshold fluences of ablation and effective absorption depths. Our results show that ablation at 157 nm happens at low fluences (0.3–0.5 J cm^{-2}) comparable with 193 nm for soda-lime glasses and calcites. For materials like calcium sulphates, quartz and fused-silica glasses, we demonstrate controlled, photochemical ablation at low fluences (0.3–1.1 J cm^{-2}). To illustrate the applicability of 157 nm laser ablation for ICP-MS measurements, a trace element map of a quartz sample with variable composition is shown. Additionally, initial, qualitative results of the ablation of water ice are shown for both 193 nm and 157 nm, which demonstrate controlled ablation behaviour even in low impurity ice at 157 nm. Overall, our results indicate that LA-ICP-MS at 157 nm is a viable analytical method for sample matrices that are near-transparent at 193 nm and thus often difficult to ablate.

1 Introduction

Over the past three decades laser-ablation inductively coupled plasma mass spectrometry (LA-ICP-MS) arguably has matured into a versatile and commonly applied technique for spatially-resolved elemental and isotopic analysis at the micrometer scale. Notable developments included the gradual decrease in the employed laser wavelengths from the IR[1] to the deep-UV and from ns to fs pulse lengths.[2–9] The wavelength transition was driven by the generally improved ablation characteristics at shorter wavelength *e.g.* ref. 7, 10 and 11. ArF excimer lasers, operating at 193 nm (deep-UV, DUV) wavelength and ns-pulse length, have by now become something close to a standard due to their excellent performance for a vast range of materials, combined with their relative ease of use.[2,5,12,13]

Using LA-ICP-MS at wavelengths shorter than 193 nm has only rarely been done, despite excimer lasers being able to generate shorter wavelengths in the vacuum-UV (VUV) such as 126 nm (Ar$_2$), 146 nm (Kr$_2$), 157 nm (F$_2$) and 172 nm (Xe$_2$).[14] Of these, only lasers operating at 157 nm are currently commercially available, and even then they are not widely used for LA-

*a*Institute of Geosciences, Goethe University Frankfurt, Frankfurt am Main, Germany. E-mail: erhardt@em.uni-frankfurt.de; w.muller@em.uni-frankfurt.de

*b*Frankfurt Isotope and Element Research Center (FIERCE), Goethe University Frankfurt, Germany

*c*Norris Scientific, Hobart, Tasmania, Australia

*d*Laurin Technic, Canberra, Australia

This journal is © The Royal Society of Chemistry 2025

J. Anal. At. Spectrom., 2025, 40, 2857–2869 | **2857**

ICP-MS. F_2 excimer lasers and the related optical components experienced a big push in their development due to their use in semiconductor manufacturing during the late 1990s/early 2000s.[15,16] Even though this 157 nm photo-lithography was mostly abandoned, many technological advances had been made and can now be capitalized on for other uses such as micro-machining of optics[17,18] or photo-ionization in secondary neutral mass spectrometry.[19,20]

To the best of our knowledge, only three LA-ICP-MS systems using 157 nm lasers have existed so far.[11,21,22] The major reason for this is the fact that delivering 157 nm radiation at sufficiently high energies to a sample surface is technically challenging, due to the very strong attenuation of VUV radiation in ambient air and on optical surfaces.[23] This is compounded by the fact that the same laser source typically delivers less than 10% of the energy at 157 nm than it would at 193 nm.

Nevertheless, for LA-ICP-MS there are some good reasons for using shorter wavelengths such as 157 nm that outweigh the challenges associated with constructing and operating VUV beam paths. The foremost reason, however, is the much greater absorption of 157 nm radiation compared to 193 nm radiation in some 'difficult to ablate' materials such as quartz, fused silica and water ice. This promises better ablation characteristics. Furthermore, photons at 157 nm carry a higher energy (7.9 eV vs. 6.4 eV at 193 nm), which can contribute to improved ablation if the energy is sufficient to overcome band gaps in the ablated material with a single-photon interaction. In natural quartz or fused silica, ablation at 193 nm is dominated by two-photon interactions, often requiring very high on-sample fluences for ablation.[5,24] For high-purity fused silica glasses much lower ablation fluence thresholds and generally much more controlled ablation behaviour have been reported for 157 nm than for 193 nm,[17,18] indicating that two-photon interactions are not required to produce ablation in quartz using this wavelength. Even though high on-sample fluences are a viable approach for quartz ablation,[5] this does not necessarily extend to all matrices that are also mostly transparent at 193 nm. The deep penetration of the 193 nm radiation into a transparent sample can lead to unpredictable ablation behavior if ablation is initiated due to changing material properties or impurity content inside the sample. Even if that is not the case, the use of large fluences can result in large ablation rates, that can rapidly penetrate thin samples, once ablation takes place. Additionally, the limited data available indicate, for example, that at 157 nm less elemental[11] and isotopic fractionation[22] is observed than at longer wavelengths.

Water ice is virtually transparent at the commonly used DUV wavelengths (193 nm and 213 nm),[25–28] which can lead to uncontrolled ablation or a dependence of the ablation behaviour on the impurity/dust content of the ice.[29] At 157 nm, the laser energy is absorbed seven orders of magnitude stronger by the ice than at 193 nm,[28] which is likely to alleviate some of the problems with laser ablation of ice, if the laser energy is absorbed by the ice itself.

In the following we outline the design and implementation of a dual-wavelength laser ablation system for both 193 nm and 157 nm ablation using two dedicated laser sources. We focus on the considerations that went into the construction and operation of the 157 nm beam delivery system relative to the more routinely used 193 nm wavelength. The implementation of the system is then characterized in terms of the energy loss along the 157 nm beam path and ultimately the laser energy transfer onto the sample. After stable and repeatable energy transmission from the 157 nm laser to the ablation cell has been demonstrated, ablation rates over a range of on-sample fluences are presented for selected samples using both 193 nm and 157 nm. These include some for which high 193 nm fluences are needed for ablation and uncontrolled ablation can sometimes be observed nevertheless. The ablation rate measurements will then be used to highlight different ablation characteristics by determining the threshold fluences of ablation (or ablation threshold) and the effective absorption coefficients for the two different UV wavelengths for each material.

To demonstrate the viability of the 157 nm LA-ICP-MS system for the analysis of challenging geological materials, initial results from a trace-elemental map of a natural quartz sample will be shown. Additionally, preliminary, qualitative results for the laser ablation of ice at 157 nm will be presented, which will be expanded upon quantitatively in a future publication. These data serve to showcase the potential of using 157 nm laser ablation for materials that are nearly transparent at DUV and are thus challenging to analyze quantitatively using DUV-LA-ICP-MS.

2 Methods and materials

2.1 General LA-system design considerations

Early in the design of the system, several fundamental decisions were made: firstly, to base the system around the RESOlution-SE (Applied Spectra Inc., USA) 193 nm laser ablation system; secondly to use an S155 two-volume ablation cell (Laurin Technic, Canberra, Australia); and finally to use two dedicated laser sources and beam paths for the two wavelengths. The open architecture of the RESOlution-SE frame lends itself to the modifications needed to accommodate a purpose-built 157 nm beam path. Its 193 nm beam delivery system, as well as the S155 two-volume ablation cell are both tried and tested. The size and performance of the S155 cell was furthermore paramount for the design of a new cryo-sample holder to hold frozen samples, for example for ice-core studies (Laurin Technic, Canberra, Australia) that will be presented in a future study, as its detailed design and performance is beyond the scope of this more general study. The overall design of the 157 nm beam path and the entire system integration was undertaken by Norris Scientific (Hobart, Australia), including the integration into the GeoStar LA software that is used to control both the 193 nm and 157 nm subsystems. Finally, the LA system is coupled to an Agilent 8900 #100 ICP-MS/MS triple-quadrupole mass spectrometer.

The choice of two rather than one laser source operated with two different excimer gases (F_2 for 157 nm and ArF for 193 nm in their respective mixtures) was made to increase laser longevity and to be able to optimize each beam path to the capabilities of either laser and their respective use cases. This design choice
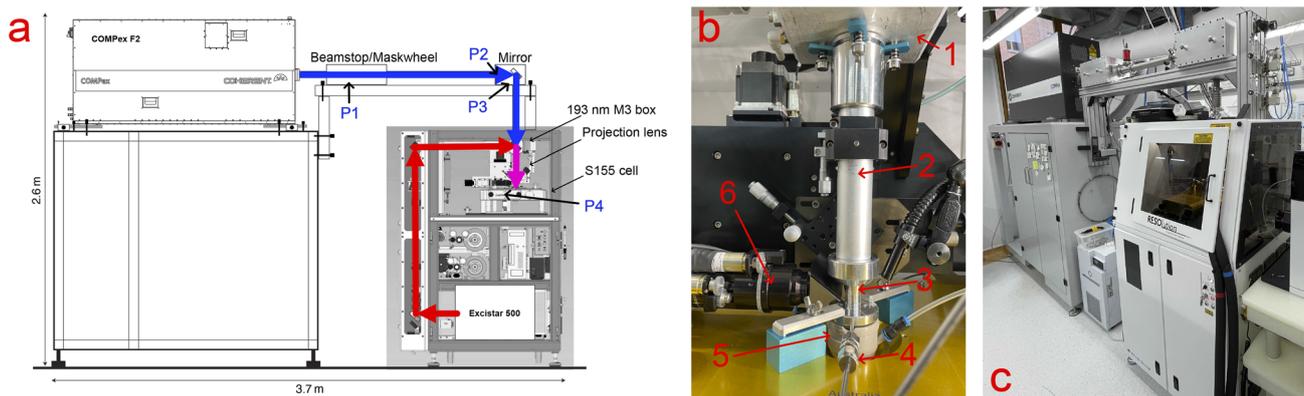
2858 | J. Anal. At. Spectrom., 2025, 40, 2857–2869

This journal is © The Royal Society of Chemistry 2025

Fig. 1 Schematic overview of the dual wavelength (157 & 193 nm) LA-ICP-MS/MS system built around the RESOlution-SE frame (a) and photographs of the 157 nm lower BDU setup (b) and the entire setup (c). The 157 nm COMPex F2 laser is elevated on a steel frame to minimize the number of optical elements needed to project the laser light onto the sample inside the S155 sample cell. In (a), the 157 nm beam path is indicated by the blue, the 193 nm path by the red and the shared beam path by the purple arrows. Measurement positions for the transmission measurements are indicated with labels P1–4 along the 157 nm beam path. In panel (b), the number components are (1) 193 nm M3 box, (2) projection lens tube, (3) transition piece to funnel, (4) purge gas inlet, (5) funnel, (6) off-axis viewing system.

makes it possible to switch between the two wavelengths relatively quickly to facilitate comparative testing, as well as increase usability in a multi-user/multi-purpose lab environment. Fig. 1 shows a schematic overview of the system as it is situated at the Frankfurt Isotope and Element Research Center (FIERCE) and photographs of the system in place, including details of the lower vertical 157 nm beam path.

For the 193 nm part of the system, the frame of the RESOlution-SE system was slightly modified to accommodate an Excistar 500 laser source (Coherent GmbH, Göttingen, Germany) which was chosen to consolidate the laser manufacturer used in the FIERCE lab. The Excistar 500 laser furthermore allows for higher repetition rates (500 Hz *vs.* 300 Hz) than the standard ATL ATLEX-I-LR laser at a maximum stabilized energy of 14 mJ. Using this laser, the 193 nm part of the system can be used for high-repetition-rate work such as fast line and raster ablations as well as routine spot analysis in various sample

matrices. The full specifications of the Excistar 500 can be found in Table 1.

2.2 157 nm beam delivery system

In order to implement a usable 157 nm laser system, the transmission of the energy from the laser onto the sample surface is the biggest challenge.[15,30] Electromagnetic radiation at 157 nm, in VUV range, is readily absorbed even by trace amounts of O_2 or H_2O as well as by the optical elements and contamination on their surfaces. The choice of substrates for optical elements is also limited to highest-purity fluorides such as CaF_2 and MgF_2. Because of the large expected losses of laser energy along the beam path due to absorption in the residual atmosphere as well as due to losses on the necessary optical elements, the laser output energy for the 157 nm laser source needs to be as high as practically possible. To the best of our knowledge, the highest-energy commercially available 157 nm laser is the COMPex F2 (Coherent GmbH, Göttingen, Germany), which is based on the COMPex 200 series, released in late 2021. With its maximum stabilized output of 32 mJ, it was chosen for the presented LA system (for more specifications see Table 1).

Starting with this laser source, the optics of the beam delivery unit (BDU) were designed with the fewest number of optical elements to minimize energy loss, while imaging the laser aperture with sufficient resolution on the target (see Fig. 1 for a schematic overview), similar to what has previously been done by Telouk *et al.*[22] To do so, the laser source is elevated above the top level of the RESOlution-SE system using a custom-made steel frame. This means, that only one mirror is needed to direct the 157 nm laser beam onto the sample from above through the modified third mirror box of the 193 nm beam path situated directly above the ablation cell. The 157 nm laser light is then focused through the window of the ablation funnel onto the sample using a single plano-convex lens. Due to this configuration, to switch between 157 nm and 193 nm operation, only the third mirror of the 193 nm beam path needs to be

Table 1 Relevant summary specifications of the Excistar and COMPex F2 lasers, as provided by Coherent. Note that the Excistar uses a special high-energy gas mix, the regular gas mix yields approximately 30% lower maximum energy. Note that the F_2 gas mixture does not contain neon as buffer gas, which typically significantly contributes to the gas costs of the ArF gas mixtures

	Excistar 500	COMPex F2
Excimer	ArF	F_2
Gas mix	0.129% F_2 rest Xe, Ar, and Ne in proprietary ratios	0.087% F_2, rest He
Wavelength (nm)	193	157
Pulse duration (ns)	7	20
Max. rate (Hz)	500	50
Max. stab. energy (mJ)	14	32
High voltage (kV)	0.8–1.4	25–30
Cooling	Air	Air, water
Beam size (mm)	5.6 × 2.2	22 × 8

This journal is © The Royal Society of Chemistry 2025

J. Anal. At. Spectrom., 2025, **40**, 2857–2869 | **2859**

reinstalled and re-aligned and the projection lens assembly needs to be swapped and refocused. The quick switch-over is further enabled by the tight integration of both subsystems into the GeoStar LA software, including for example wavelength specific fluence calibrations and control of the 157 nm BDU vacuum and purge systems.

All optical elements of the 157 nm BDU, namely the mirror, the plano-convex projection lens ($r_1 = 43$ mm, thickness 6 mm) and the cell/funnel window are made of '157 nm excimer-grade' CaF substrate with 157 nm specific coatings (Laseroptik GmbH, Garbsen, Germany). CaF_2 was chosen over MgF_2 due to the isotropic optical properties. The 157 nm BDU presently does not have any beam-shaping optics or a beam attenuator to keep the design as simple as possible and energy losses at a minimum. As a laser aperture, the system uses a standard 20-position mask wheel (Applied Spectra) with round and square spots ranging from 6 μm to 228 μm in diameter on the sample after demagnification by 25×.

As mentioned above, ambient air is highly absorbing for VUV light. At 157 nm, the absorption coefficients of O_2 and H_2O are 140 cm^{-1} and 64 cm^{-1} (base e) respectively,[31,32] leading to an extinction length of 157 nm radiation in ambient air of less than a mm. That implies that the beam path must be essentially free of either O_2 and H_2O to achieve any meaningful energy transmission onto the sample. As an additional complication, even trace levels of hydrocarbons in the beam path are known to create highly absorbing surface contamination on optical surfaces due to their reaction with the VUV light.[33] This means, that in order to transmit the 157 nm light efficiently through the BDU, the entire beam path needs to be encapsulated and either purged with a suitable gas or evacuated.[23] However, to be able to use the beam path under vacuum, very high vacuum levels are needed to achieve low enough levels of contamination to keep the optics from rapidly degrading due to the long mean free path at pressures low enough for good transmission.[33] This requirement would pose significant challenges for the construction and the operation of the beam path, leading to the implementation of the alternative method of purging the beam path with a clean gas. Here high-purity nitrogen (99.9999%, Nippon Gas) is used as a more cost-effective alternative to Ar, which was successfully used in the previous 157 nm LA-ICP-MS systems.[11,22]

The beam path from the laser to the sample is effectively split into two distinct parts by the funnel window that separates the BDU from the ablation cell. Within the ablation cell, the laser beam passes through the stratified Ar/He atmosphere used for ablation and aerosol transport, which both do not absorb 157 nm light.[22,23] The sample cell itself is already constructed to be evacuated and backfilled in routine operation to remove any air from the ablation environment. Together that means that the short beam path through the sample cell is not a major concern, leaving the much longer BDU as the main hurdle for the light transmission onto the sample. As a side note, at 157 nm even tiny leaks in the gas supply to the LA cell or in the cell itself will lead to the entire laser energy being absorbed over the short distance it travels from the top of the funnel to the sample.

The BDU between the laser output flange and the funnel window is constructed from a mix of off-the-shelf and custom-machined aluminium or stainless-steel parts. To join the different parts of the BDU standard KF40 flanges and stainless-steel bellows were used wherever possible. This includes the laser output flange, which is also a KF40 vacuum flange, making the connection to the laser vacuum tight. During testing of the beam path, it became evident that stable and repeatable energy transmission could only be achieved after all surfaces inside the beam path had been stripped back to bare metal surfaces (including mounts for the optical components) due to desorption of contaminants from anodised surfaces. Additionally, it is important to avoid any contamination of the surfaces of the beam path during handling and adhere to extensive cleaning protocols for any new parts. For all other joints especially in the vertical BDU that connect the projection lens tube with the funnel of the LA cell, custom-machined parts with Viton O-rings where used. The lower vertical BDU is shown in the bottom right picture in Fig. 1b; note, that the beam path here is entirely encapsulated, whereas the 193 nm beam would pass through air above and below the projection lens assembly. Sample viewing at 157 nm is identical to that at 193 nm: The microscope (6) views the sample at an angle of 10–15 degrees from the vertical by way of a mirror and the CaF_2 cell window. The reflected light is admitted at a commensurate angle on the opposing side of the transition piece (3) which has cutouts for illumination and viewing. Special care was also taken to shield all O-rings from direct and scattered laser light. The nitrogen purge gas for the BDU is introduced at both ends of the BDU, namely *via* the purge gas inlets at the resonator window and internal energy meter of the laser as well as at the top surface of the funnel window. In this way, the BDU is purged from two sides, with the volumetric flow rates for each purge inlet set using rotameters. Wherever possible, the tubing used for the purge gas is internally electropolished stainless steel to avoid contamination by hydrocarbons from plastic tubing.

Initially, it was envisaged to evacuate the beam path using the membrane vacuum pump of the ablation cell before backfilling with N_2 after opening of the beam path. With this setup a base pressure of about 10–20 hPa could be reached. However, during initial testing it was found that (1) lower vacuum levels were needed for backfilling than the pump could achieve in reasonable time and (2) that running the purge gas and the vacuum pump at the same time yielded higher transmission numbers. The vacuum pump on the system was subsequently changed to an oil-free scroll-type vacuum pump (HiScroll6, Pfeiffer) and a Pirani pressure gauge (PPT200, Pfeiffer) was added to the beam path to be able to monitor the lower pressures. Using this pump, the roughly 20 l beam path can be evacuated down to sub-1 hPa pressures prior to backfilling with the nitrogen purge gas. During purging, the pump is then used to vent out the gas, which results in a pressure inside the beam path around 70 hPa while purging at a total N_2 flow of 10 l min^{-1} split equally to the two purge inlets. This serves two purposes: Because the pump is used to vent the purge gas, back-diffusion of contaminants through a vent port into the beam path is avoided. Additionally, the lower pressure inside the beam path yields higher transmission due to the lower number of contaminant molecules in the beam path, while the pressure is still high enough, *i.e.* the mean free path short enough, to

2860 | *J. Anal. At. Spectrom.*, 2025, **40**, 2857–2869

This journal is © The Royal Society of Chemistry 2025

avoid contamination of the optics. A similar approach has been taken for another 157 nm beam delivery system used for single-photon ionization.[19,34] Furthermore, an optical O_2 sensor (OXYPro, PreSens, Regensburg, Germany) can be used to monitor oxygen levels inside the BDU, which can be indicative of leaks both real or virtual.

2.3   157 nm energy transmission measurements

To assess the transmission performance we performed a range of laser energy measurements to characterize the energy loss along the 157 nm beam path and to gauge the long-term stability of the on-sample fluence under realistic measurement conditions. These measurements are facilitated by the ability to mount a standard pyroelectric laser energy meter (EnergyMax, Coherent) at different locations in the BDU as well as inside the sample cell without compromising the atmosphere inside either the BDU or the sample cell. This is achieved by using vacuum-rated feedthroughs for the energy meter cable to the BDU and sample cell and by adding mounting positions at strategic locations along the BDU (Fig. 1a).

Along the BDU, the energy was measured at three locations after the laser output, successively adding additional sources of energy loss before the final measurement inside the laser ablation cell, where a sample would be mounted. The measurement locations for the transmission along the beam path are indicated by labels P1–4 in the schematic overview in Fig. 1a. The measurements were performed relative to the internal energy meter of the laser, however, normalizing the overall transmission to the measurement taken behind the mask wheel (MW, P1). In this way, any discrepancy between the internal and the external energy meter can be eliminated. All measurements were performed with the biggest available laser aperture (5.7 mm circle), and the maximum laser high-voltage (30 kV) to provide the highest total energy for the energy meter. This also maximizes the volume that is swept by the laser light and thus the sensitivity for absorption by any residual contaminants in the BDU. Measurements were performed after the MW (P1), as the reference position, after the horizontal beam tube ahead of the mirror (P2), 103 cm along the beam path, after the mirror (P3) and finally inside the ablation cell (P4). The transmission measurements at multiple locations allow us to assess the energy loss due to residual contaminants in the BDU (P2 *vs.* P1), due to the mirror (P3 *vs.* P2) and due to the complete vertical BDU (P4 *vs.* P3), including the projection lens, funnel window and sample cell.

Following the standard procedures used after BDU venting and during operation of the laser, the BDU was pumped down to 1 hPa and backfilled with N_2 after the energy meter was installed at the respective location. The purge gas was then run for 2–3 minutes before the laser was fired at 10 Hz to perform the measurement. During the measurement the pressure inside the BDU settles around 70 hPa for a total N_2 purge rate of 10 l min^{-1}. Inside the sample cell the measurement of the on-sample fluence was performed after a standard sample-exchange procedure with repeated evacuation/backfilling of the cell with He and Ar flows akin to what are routinely used for

LA-ICP-MS measurements in our lab (350 ml per min He, 900 ml per min Ar). These gas flows are required to keep the beam path clean of any contaminants from sample or cell that outgas or form during the VUV irradiation. The exact flow rates do not play a major role in the transmission as long as the flows are high enough to keep the beam path inside the cell clean.

In addition to these measurements, the repeatability of the on-sample fluence after a sample exchange was assessed by repeating the exchange procedure multiple times and measuring the transmitted energy. Furthermore, the long-term stability of the transmission was evaluated by simulating a typical measurement session with the energy meter inside the ablation cell. This test was done by using the laser in energy-stabilized mode at an energy equivalent to 3 J cm^{-2} on sample, going through a repeated cycle of firing at 10 Hz for 60 s with a 60 s simulating 240 spot ablations over 8 h.

2.4   Ablation rate measurements

To investigate the difference in terms of ablation behaviour between 193 nm and 157 nm, we determined the ablation rates at different laser fluences for a range of materials at both wavelengths. The materials chosen include some with poor ablation characteristics at 193 nm, besides some regular standard materials. Specifically, we investigate the standard reference materials NIST SRM610, SRM612 and SRM614, and several natural crystalline materials sourced in-house at FIERCE, the mineral collection at Goethe University or other sources as indicated. These materials include two gem quality calcites ($CaCO_3$), modern *Tridacna* (aragonitic giant clam, $CaCO_3$), gem-quality anhydrite ($CaSO_4$), gem-quality gypsum ($CaSO_4 \cdot 2H_2O$), baryte ($BaSO_4$), four different quartzes (SiO_2), several natural fluorites (CaF_2) several potassium salts (carnallite, $KMgCl_3 \cdot 6H_2O$; sylvite, KCl; polyhalite, $K_2Ca_2Mg[SO_4]_4 \cdot 2H_2O$, all from the former Morsleben repository for radioactive waste Germany) as well as two types of high-purity fused silica glass (Suprasil and Herasil, Heraeus, Germany). At both wavelengths, the ablations for the rate measurements were performed at 10 Hz for 300, 600 and 900 pulses and a range of fluences from 1 to 5 J cm^{-2} at spot sizes of 104 μm for 157 nm and 80 μm for 193 nm. On sample fluence for 193 nm were set using the on-sample fluence calibration available in the GeoStar LA software to fluences from 1 to 7.6 J cm^{-2}. For 157 nm, the ablations were performed in the constant high-voltage mode of the laser, spanning the range of discharge voltages from 25 to 30 kV and performing an on-sample fluence calibration measurement before and after each ablation session. Because the available range of output energy of the COMPex F2 is not large enough to cover the full required fluence range and because there is presently no beam attenuator in the 157 nm BDU, most of the experiments at 157 nm were performed in up to three sessions, on different days and at different laser performance levels.

The depths of the resulting craters were then determined using an optical digital microscope (Keyence VHX) in triplicate. Measured crater depths were evaluated using a model following Herman *e.g.* ref. 17 that relates the ablation depth D for a given

This journal is © The Royal Society of Chemistry 2025

J. Anal. At. Spectrom., 2025, **40**, 2857–2869 | 2861

number of laser shots N at a given fluence F to obtain sample/wavelength specific values of the threshold fluence of ablation F_t and an effective absorption coefficient α_{eff}:

$$D = N \frac{1}{\alpha_{\text{eff}}} \ln\left(\frac{F}{F_t}\right). \tag{1}$$

In this way, the material- and wavelength-specific values of F_t and α_{eff} can be used to compare the ablation rates of the different materials over the entire range of fluences, instead of directly comparing ablation rates. It is worth noting, that the effective absorption coefficient in this model is not equal to the linear absorption coefficient of the material at that specific wavelength, as it is influenced by other factors such as surface roughness or transient effects during the high fluence interaction of the light with the sample.[17] Furthermore, this model can only be applied if controlled, photochemical ablation takes place without fracturing of the sample.

Posterior samples of the model parameters were obtained within a Bayesian framework using Hamiltonian Monte Carlo sampling.[35] All parameter estimates in the paper are provided as marginal posterior medians and parameter uncertainties as 2.5 and 97.5% marginal posterior percentiles, if not otherwise noted.

2.5 Trace elemental mapping of natural quartz using 157 nm

To gauge the stability and repeatability of the ablation at 157 nm ablation, a trace element map of a natural quartz sample was acquired. The raster ablation was performed at an on-sample fluence of 2.0 J cm^{-2} using a 48 μm rectangular spot and 48 μm line spacing center-to-center, with the laser being triggered by a QuadLock device[36] to avoid aliasing artifacts. The scan speed for the analysis was 59.464 μm s^{-1} (12 μm per sweep). Each line was pre-ablated just prior to ablation using the same spot size and an overlap of 75% between spots, to avoid cross-contamination from the ablation blanket of the previously ablated adjacent line. This approach differs from previous studies[37,38] that used wide gaps between lines for the same purpose, and provides full coverage of the investigated area. The ICP-MS measurements were acquired using an Agilent 8900 ICP-MS/MS operated in single quadrupole mode with the sample introduced using the factory sample introduction system with a single pulse response of 800 ms (FW0.1M). A range of 14 masses were acquired of which only aluminium, lithium and gallium are shown here as they showed the largest compositional variability. The plasma conditions were optimized for robustness, so that <0.1% ThO/Th, <0.2 % Ca^{++}/Ca$^+$ and Th/U of ~1 on NIST612, further measurement parameters can be found in Table 2. The data were combined by averaging four consecutive MS sweeps, such that the final resolution of the image is 48 μm. Abundances were calculated from the background corrected signals using ^{29}Si as internal standard assuming 0.99 g per g SiO$_2$ in the sample using NIST SRM612 as calibration standard, overall following Longerich *et al.*[39] We note that this ignores any variability of the SiO$_2$ content inside the map introducing additional, likely systematic uncertainties into the quantified abundances that is not accounted for. NIST SRM610 and MPI-DING

Table 2 Data acquisition parameters used for the 157 nm elemental mapping. Note that not all acquired isotopes are shown here.

ICP-MS/MS	Agilent 8900 #100
RF power	1350 W
Sampling depth	5.0 mm
Sample gas	1.00 l min^{-1}
H$_2$	5.0 ml min^{-1}
Dwelltimes	^{7}Li: 10 ms, ^{27}Al: 10 ms, ^{29}Si: 5 ms, ^{71}Ga: 20 ms
Sweeptime	201.8 ms
Mode	Single quadrupole
Laser ablation	Dual wavelength system
Laser	COMPex F2
Wavelength	157 nm
On-sample fluence	2.0 J cm^{-2}
Spotsize	48 μm square
Repetition rate	49.55 Hz (10 per sweep)
Scan speed	59.464 μm s^{-1} (12 μm per sweep)
He	350 ml min^{-1}

GOR128-G were measured under the same conditions to serve as quality control. The measured average values agree within uncertainties with the published values[40,41] and are given here with 2-σ uncertainties from the pixel-to-pixel variance and relative deviations from the published values in parentheses. For NIST SRM610: Li: 473 ± 14 μg g^{-1} (+1%); Al: 10 389 ± 126 μg g^{-1} (+0.6%); Ga: 434 ± 17 μg g^{-1} (+0.2%) and for MPI-DING GOR128-G: Li: 11 ± 1 μg g^{-1} (+5.7%); Al: 52 541 ± 690 μg g^{-1} (+0.1%); Ga: 9 ± 0.4 μg g^{-1} (+3.8%). All references materials where measured prior and after the line ablations for the map.

2.6 Ablation of ice at 157 nm

To qualitatively test the ablation of ice, a sample of the Greenland ice from the last glacial period was used (EGRIP ice core, approximately 14.7 ka before 2000 AD).[42] Additionally, ablation tests were performed on high purity water (mQ, Merck) frozen in an acid-cleaned PTFE container. The sample was prepared by scraping the surface flat with an ZrO$_2$ ceramic blade (Fortisblades, Zwevegem, Belgium), on a PTFE surface over a liquid nitrogen reservoir inside a laminar flow hood to prepare a flat, fresh surface for ablation (following Della Lunga *et al.*[43]). The cryo holder is pre-chilled to −30 °C in a chest freezer prior to mounting of the sample. Inside the S155 ablation cell the holder is cooled by circulating chilled ethanol (80%) at −30 °C through the holder. To test the quality of the ablation, tracks with an approximate length of 1 cm were ablated into the ice, crossing a grain boundary that was visible under the laser camera. The laser was triggered using the QuadLock to fire 10 times each MS sweep (223 ms for 193 nm and 214 ms for 157 nm), while scanning half of a spotsize (50 μm for 193 nm and 48 μm for 158 nm) resulting in repetition rates of 44.84 Hz and 46.74 Hz with a scan speed of 112.11 μm s^{-1} and 112.15 μm s^{-1} respectively. Fluences where 6.5 J cm^{-2} for 193 nm and 1.5 J cm^{-2} for 157 nm. These settings were chosen such that the repetition rate of the 157 nm laser is below its maximum repetition rate of

2862 | *J. Anal. At. Spectrom.*, 2025, **40**, 2857–2869

This journal is © The Royal Society of Chemistry 2025

50 Hz and to mimic analytical track ablations of ice-core samples with a total track depth of 20 laser shots. Further details about holder design and the accompanying sample preparation and measurement procedures will be presented in a future publication. To assess the quality of the ablation the resulting tracks were examined under laser camera for irregularities such as ragged edges.

3 Results and discussion

3.1 157 nm transmission

In our overall transmission tests with the 5.7 mm aperture (corresponding to a 228 μm diameter spot on sample), approximately 54% of the total laser energy is transmitted through the entire BDU onto the sample, resulting in measured on-sample fluences of around 6 J cm^{-2} for a laser output of 31.5 mJ. Due to the still slightly uneven energy distribution of the beam and because the 5.7 mm-aperture is close to the nominal width of the beam, the apparent transmission value increases with decreasing spot size. For example with a 2.6 mm aperture (104 μm spot), on-sample fluences increase to 8 J cm^{-2} at 32 mJ laser output energy. This effect is accounted for by the fluence calibration in the GeoStar LA software. The on-sample fluences are stable to within 3–5% (1σ) after opening, venting and the sample-exchange backfill procedure.

The detailed energy/transmission measurements along the BDU allow us to gauge the sources of the overall energy loss: in these measurements the atmospheric absorption in the BDU attenuates 10% of the energy per meter, with an absorption coefficient of 0.001 cm^{-1} (base e) at the 70 hPa pressure inside the BDU using the high-purity N$_2$ purge. The reflectivity of the mirror is close to or better than 99% with the measurement limited by the precision of the energy meter. Most of the energy loss in the BDU occurs along the vertical beam path that includes the projection lens and LA cell window. Along the vertical BDU, the transmission is only about 60% which, assuming a well mixed atmosphere in the 1 m beam path, means that the optical elements only transmit about 67% of the laser energy. This would translate into a relatively high loss of 18% of energy at each of the optical elements, well outside the specifications of the optics. However, it is also possible that the atmosphere in the vertical path of the BDU or inside the ablation cell is not as transmissive as measured in the horizontal part of the BDU: The lower vertical BDU includes two sliding seals to accommodate a motorized laser focus which could be the cause for a very small air leak into the beam path. In this case, the estimated losses on the optical elements are likely too high, which seems probable as a clean and previously unused set of optics was used for these measurements. The S155 cell itself is built to vacuum specifications including all internal components and lubricants which implies, that the atmosphere inside the cell is likely clean enough to pass the VUV radiation. At this stage, the exact cause for the large energy losses along the vertical BDU is still unknown, however the overall transmission of the BDU is very good. In fact, the limit for many of the ablation rate experiments has been the limited range of the laser output energy, not the performance of the BDU itself.
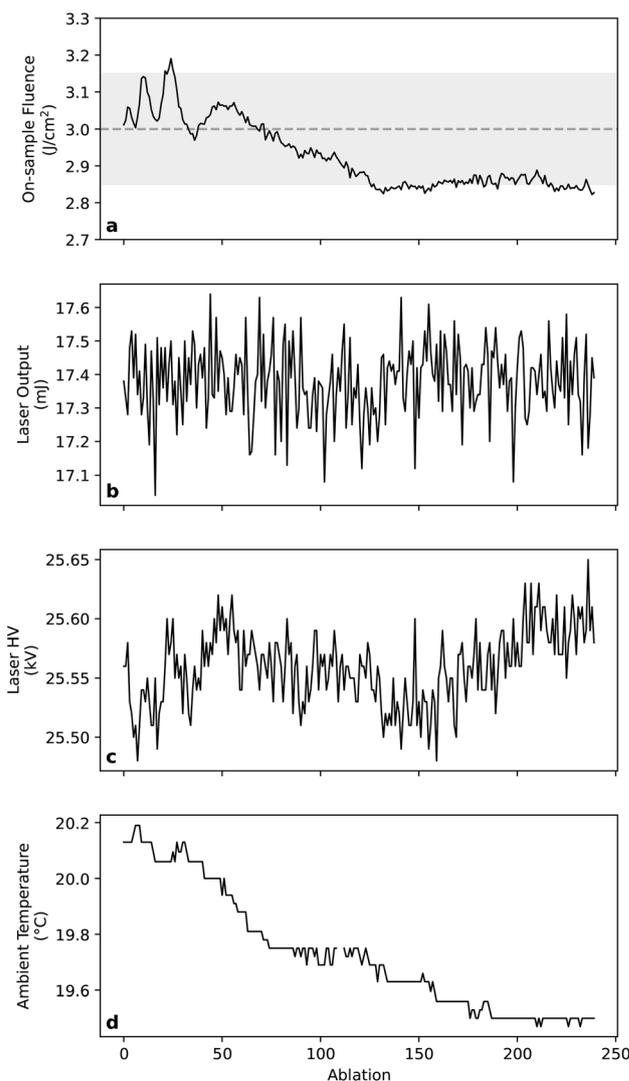

Fig. 2 On-sample fluence measurements over the course of 8 h of simulated spot ablations (a), laser output energy (b), laser HV (c) and ambient temperature (d). Ablations were performed in energy-stabilized mode for a target fluence of 3 J cm^{-2}, at 10 Hz for 60 s with 60 s breaks. The target fluence and a ±5% envelope are indicated in panel (a) by the dashed line and gray shading. The fluctuations of the on-sample fluence are likely caused by changes in the vent temperature of the air conditioning in the lab affecting the internal energy meter.

For routine measurements, the stability of the transmission and thus the on-sample fluence plays an important role. Fig. 2 shows the result of a long-term stability test with a simulated session of typical 60 s-spot ablations (plus 60 s background measurement) at a given on-sample fluence over the course of 240 ablations or a total time of 8 h. During this test, the fluence measured by the energy meter inside the ablation cell remained mostly within 5% of the set fluence of 3 J cm^{-2}, with only a few excursions outside this range. However, there are some short-term fluctuations in the beginning of the session and a long term drift towards slightly lower on-sample fluences until about 120 ablations. After this, the measured fluence settled to a constant level until the end of the test. The fluctuations of the

on-sample fluence are likely not caused by changes in the BDU transmission, but rather by the laser's internal energy meter being affected by the laboratory's ambient temperature and specifically the vent temperature of the air conditioning which is not visible in the temperature log. This is due to the fact that the temperature sensor is mounted on the horizontal part of the BDU, about 1 meter away from the laser itself. Depending on ambient and material temperature changes and the resulting changes in the mechanical loading on the internal energy meter assembly, its readings can be changed slightly. Because the laser is operated in energy-stabilized mode for the test, the erroneously changing energy reading will be compensated by the laser by adjusting the high voltage, resulting in the observed change in the on-sample fluence. This is clearly visible in the changing HV setting on the laser throughout the first half of the session. In the second half of the simulated session, the on-

sample fluence is constant, albeit at a level ~5% lower than the set point, with the laser compensating for the declining performance of the gas fill by slowly increasing the HV setting. This part of the session took place after hours, without activity in the laboratory, especially without opening and closing of the
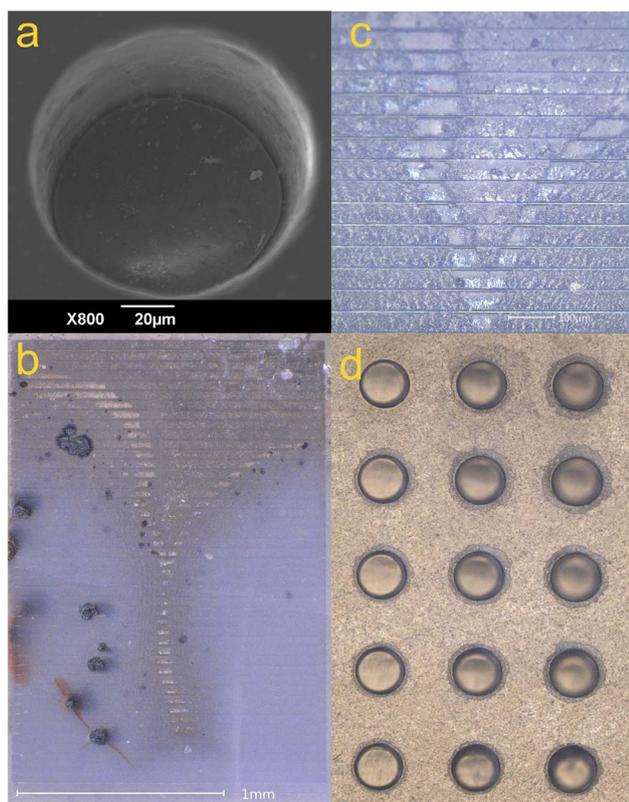
Fig. 3 (a) SEM image of a 157 nm ablation crater in natural quartz. The crater was produced with 900 shots of 2.1 J cm^{-2} and a diameter of 104 μm. The crater has a depth of 54 nm, as measured by optical microscope. (b) Optical microscope image of the area mapped for data Fig. 5 after ablation. The area covers the transition from rose-colored (top) to milky (bottom) with a clear transition area. The quartz contains a number of mineral inclusions that are visible in dark gray on the left side. (c) Detail from the mapped area, with 48 μm wide laser tracks. Note, that even though the tracks are not spaced apart from each other, a small ridge is formed at the side of each track due to the energy falloff of the laser spot. This ridge is exaggerated by the optical microscope image. (d) Multiple 104 μm spot ablations in fused silica glass at different fluences and pulse counts using the 157 μm laser. Pulse counts are 300, 600 and 900 from left to right, with increasing laser output energy from top to bottom.
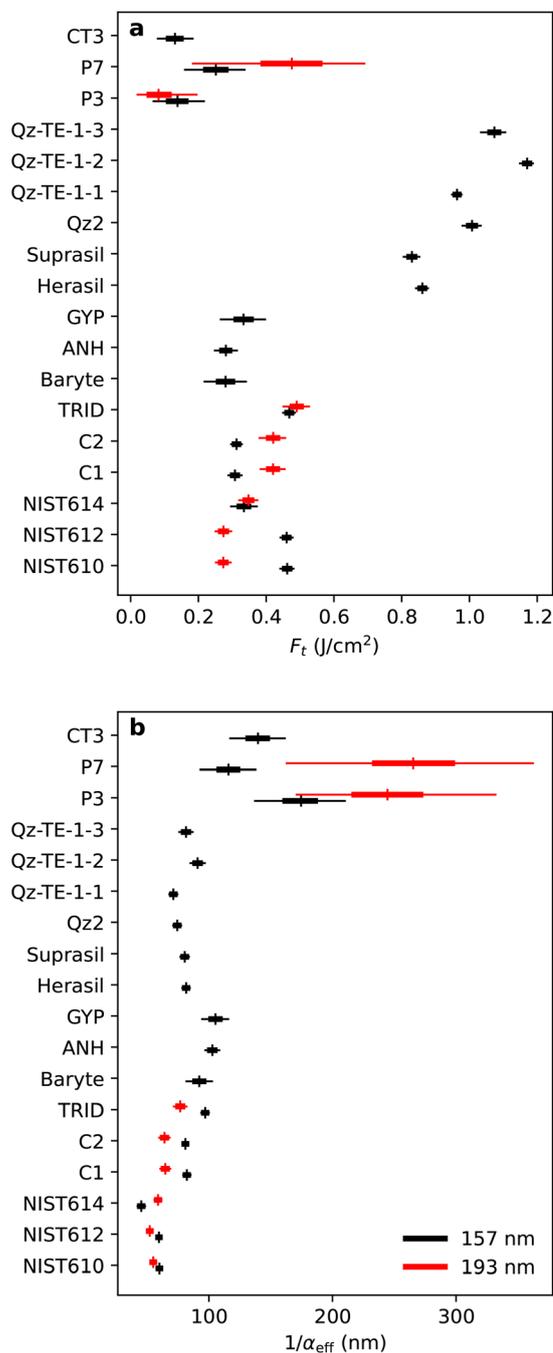
Fig. 4 Ablation model parameters determined from the crater depths after ablation at different fluences. (a) Threshold fluence of ablation and (b) absorption depth (inverse of effective absorption coefficient) for the samples that exhibited controlled ablation at 193 nm (red) and 157 nm (black). Vertical bars are the marginal posterior median values, horizontal bars denote the parameter uncertainty as marginal posterior (2.5, 25, 75 and 97.5)% percentiles. Numerical values are provided in Table 3.

2864 | J. Anal. At. Spectrom., 2025, 40, 2857–2869

This journal is © The Royal Society of Chemistry 2025

doors, which could have affected the temperature stabilization and air circulation system. Nevertheless, the overall long-term stability of the on-sample fluence is adequate for the use of the system for day-long measurement sessions and no effects of degrading optics or accumulation of absorbing substances in the BDU have been observed. That being said, the temperature effect on the internal energy meter merits further investigation and improvement, by *e.g.* shielding the laser and/or parts of the BDU from air flows in the lab.

3.2 Ablation rates at 157 nm and 193 nm wavelengths

Given the repeatable and stable energy transmission onto the sample at 157 nm, it is possible to investigate the ablation characteristics of different materials at both 193 nm and 157 nm wavelengths. The determination of the ablation rates and their subsequent evaluation in terms of ablation fluence threshold and effective absorption coefficients is only possible for controlled photochemical ablation. As expected, controlled ablation was only observed for a subset of samples of which the results will be presented in the following. At 193 nm none of the SiO_2 samples (quartz, fused silica) showed consistent clean ablation. Typically, for the analysis of quartz much higher 193 nm fluences are used, here the fluences were chosen deliberately low to maintain comparability with the 157 nm system. The same is true for all the CaF_2 samples at 157 nm. This is expected as these materials are used as substrates for 193 nm (SiO_2) or 157 nm (CaF_2) optics and are necessarily highly transparent at the respective wavelengths. In this case, any ablation at the comparatively low fluences used here is likely either controlled by impurities/defects in the crystal structure or possibly (heat-) stress accumulation in the sample during ablation leading to uncontrolled ablation. The sulfate samples – anhydrite, gypsum and baryte – also did exhibit uncontrolled ablation at 193 nm under the tested conditions. Consequently, the quantitative comparison of the ablation characteristics between the two wavelengths is only possible for the NIST glass reference materials, the aragonitic *Tridacna* sample, the calcites and the potassium salts. Fig. 3 displays a representative scanning electron microscope (SEM) image of an ablation crater in natural quartz, produced by the 157 nm LA-system at a fluence of 2.1 J cm^{-2}. It also shows two optical microscope images of the area mapped on the natural quartz sample with the 157 nm laser. Generally, the craters from the ablation at 157 nm are well-defined and have flat bottoms, and the line ablations that make up the mapping in Fig. 5 are also well-defined and do not show any signs of destructive ablation.

Fig. 4 shows the model parameters of (eqn (1)), the threshold fluence of ablation (F_t) and the inverse of the effective absorption coefficient (α_{eff}^{-1}), the absorption depth or *e*-folding depth of the laser energy inside the material. Both values together determine the ablation rate of the samples at a given fluence. Numerical values and uncertainty ranges for the parameters are provided in Table 3.

The investigated samples can be grouped into five different groups by their mineral/chemical composition, namely silicon dioxides, sulphates, soda lime glasses, carbonates and potassium salts. Between these groups, differences in the ablation characteristics tend to be larger than within each of the groups,

Table 3 Ablation model parameters shown in Fig. 4, given are marginal posterior medians with a 95% marginal posterior percentile range as uncertainty. Upper and lower values are provided to account for the slightly non-symmetric errors in some of the parameters. F_t is the threshold fluence of ablation, α_{eff}^{-1}, is the inverse of the effective absorption coefficient, denoting the *e*-folding depth of the laser energy inside the sample. Both parameters determine the ablation rate of a sample at a given laser fluence, following eqn (1)

		157 nm		193 nm	
	Type	F_t (J cm^{-2})	α_{eff}^{-1} (nm)	F_t (J cm^{-2})	α_{eff}^{-1} (nm)
CT3	Carnallite	$0.13^{+0.05}_{-0.05}$	$139.8^{+21.7}_{-22.5}$		
P7	Polyhalite	$0.25^{+0.09}_{-0.09}$	$116.1^{+22.5}_{-23.4}$	$0.48^{+0.21}_{-0.29}$	$265.3^{+96.9}_{-102.4}$
P3	Sylvite	$0.14^{+0.08}_{-0.07}$	$174.1^{+34.4}_{-36.4}$	$0.08^{+0.11}_{-0.06}$	$244.5^{+87.4}_{-73.5}$
Qz-TE-1-3	Natural quartz	$1.07^{+0.03}_{-0.04}$	$81.5^{+5.4}_{-5.4}$		
Qz-TE-1-2	Natural quartz	$1.17^{+0.02}_{-0.02}$	$90.9^{+5.9}_{-5.7}$		
Qz-TE-1-1	Natural quartz	$0.96^{+0.01}_{-0.01}$	$71.2^{+3.3}_{-3.3}$		
Qz2	Natural Quartz	$1.01^{+0.03}_{-0.03}$	$74.4^{+3.2}_{-3.2}$		
Suprasil	Fused silica	$0.83^{+0.02}_{-0.02}$	$80.5^{+3.4}_{-3.4}$		
Herasil	Fuse silica	$0.86^{+0.02}_{-0.02}$	$81.6^{+3.0}_{-3.0}$		
GYP	Gypsum	$0.33^{+0.06}_{-0.07}$	$105.3^{+10.3}_{-10.8}$		
ANH	Anhydrite	$0.28^{+0.03}_{-0.03}$	$102.8^{+5.6}_{-5.7}$		
Baryte	Baryte	$0.28^{+0.06}_{-0.06}$	$92.4^{+10.0}_{-10.4}$		
TRID	Aragonite	$0.47^{+0.02}_{-0.02}$	$97.0^{+3.0}_{-3.2}$	$0.49^{+0.04}_{-0.04}$	$76.8^{+5.1}_{-5.1}$
C2	Calcite	$0.31^{+0.02}_{-0.02}$	$81.0^{+2.4}_{-2.4}$	$0.42^{+0.04}_{-0.04}$	$64.1^{+4.1}_{-4.3}$
C1	Calcite	$0.31^{+0.02}_{-0.02}$	$82.2^{+3.0}_{-2.9}$	$0.42^{+0.03}_{-0.04}$	$64.7^{+4.0}_{-4.0}$
NIST614	Soda-lime glass	$0.33^{+0.04}_{-0.04}$	$45.3^{+3.1}_{-3.0}$	$0.35^{+0.03}_{-0.03}$	$58.9^{+2.8}_{-2.9}$
NIST612	Soda-lime glass	$0.46^{+0.02}_{-0.02}$	$59.6^{+1.9}_{-1.9}$	$0.27^{+0.02}_{-0.02}$	$52.2^{+2.4}_{-2.4}$
NIST610	Soda-lime glass	$0.46^{+0.02}_{-0.02}$	$60.0^{+2.2}_{-2.3}$	$0.27^{+0.02}_{-0.02}$	$55.0^{+2.4}_{-2.4}$

This journal is © The Royal Society of Chemistry 2025

J. Anal. At. Spectrom., 2025, **40**, 2857–2869 | **2865**

and of these material groups, the silicon dioxides, sulphates and some of the potassium salts only showed controlled ablation at 157 nm.

Starting with the materials that only showed fully controlled ablation at 157 nm, the silicon dioxides exhibit the highest ablation threshold fluences of all investigated samples with around 1 J cm^{-2} and mid-range absorption depths around 80 nm. These values are within the range of the value reported for the ablation of fused silica glass at 157 nm[44] of ~1 J cm^{-2} and ~59 nm, where the differences are likely due to the different surface roughness or the optical setup of the beam delivery system.[18] The sulphates have very low ablation threshold fluences around 0.3 J cm^{-2}, with high absorption depths above 90 nm. This combination results in high ablation rates also at low fluences, that in turn resulted in deeper, difficult to measure craters, leading to comparatively large parameter uncertainties. The deeper penetration of the laser energy in these samples also results in a higher sensitivity of the ablation rate on the fluence compared to the other materials.

The materials that could be evaluated at both wavelengths include the NIST SRM soda-lime glasses, the carbonates and two of the potassium salts. Of the potassium salts, the craters in carnallite where too deep to measure under the optical microscope. At both wavelengths, the carbonate samples show a similar pattern between them, with the aragonitic *Tridacna* shell sample having a higher threshold fluence of ablation and a deeper laser light penetration than the visually more transparent gem-quality calcites crystals. For the aragonitic sample, the threshold fluences at both wavelengths are indistinguishable, however, at 157 nm the energy absorption in the sample is less strong. At both wavelengths, the two calcites have very similar ablation parameters, however the threshold fluence at 157 nm is ~25% lower than at 193 nm, with similarly higher penetration depths at 157 nm, leading to generally higher ablation rates at 157 nm than at 193 nm at the same fluence.

The potassium salts exhibited the highest absorption depths among the tested materials at either wavelengths, resulting in very high ablation rates – particularly at 193 nm, where rates reached up to 1 µm per shot for sylvite at a fluence of 3.5 J cm^{-2}. The resulting crater depths even exceeded those observed in the sulfate samples, contributing to large uncertainties in the derived parameters. For carnallite, crater bottoms could not be detected at 193 nm, even at the lowest tested fluence (1.5 J cm^{-2}) and shot count (300 shots). Carnallite and sylvite exhibited the lowest threshold fluences across all investigated materials at both 157 nm and 193 nm (0.14 J cm^{-2} and 0.08 J cm^{-2} respectively). Polyhalite, a potassium sulfate, showed a threshold fluence of 0.25 J cm^{-2}, comparable to that of baryte, gypsum, and anhydrite at 157 nm, and to the calcites at 193 nm. While polyhalite demonstrated fully controlled ablation at both wavelengths, carnallite and especially sylvite exhibited slightly irregular crater edges at 193 nm, even at the lowest applied fluence of 1.5 J cm^{-2}. In contrast, ablation at 157 nm was fully controlled for all potassium salts across the studied fluence range.

Finally, the different NIST SRM soda-lime glasses show a notable difference both between the different level of trace

elements (decreasing from SRM610 to SRM614) and between the two wavelengths. Most notably, at both wavelengths, NIST SRM610 and NIST SRM612 ablate very similarly with lower ablation thresholds for 157 nm and less absorption than at 193 nm. NIST SRM614 however exhibits completely different behaviour, with similar ablation thresholds for both
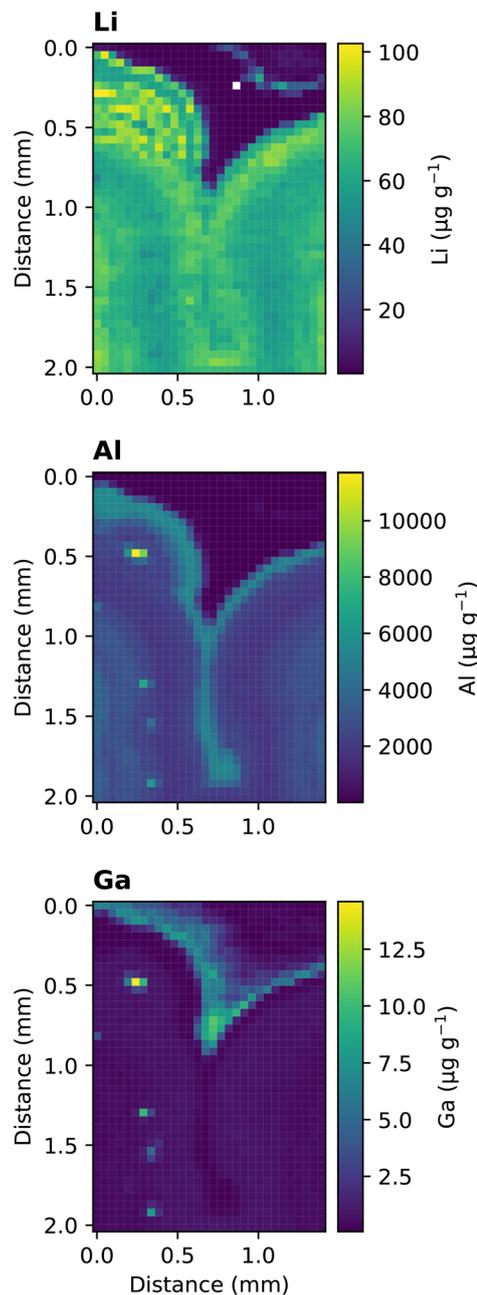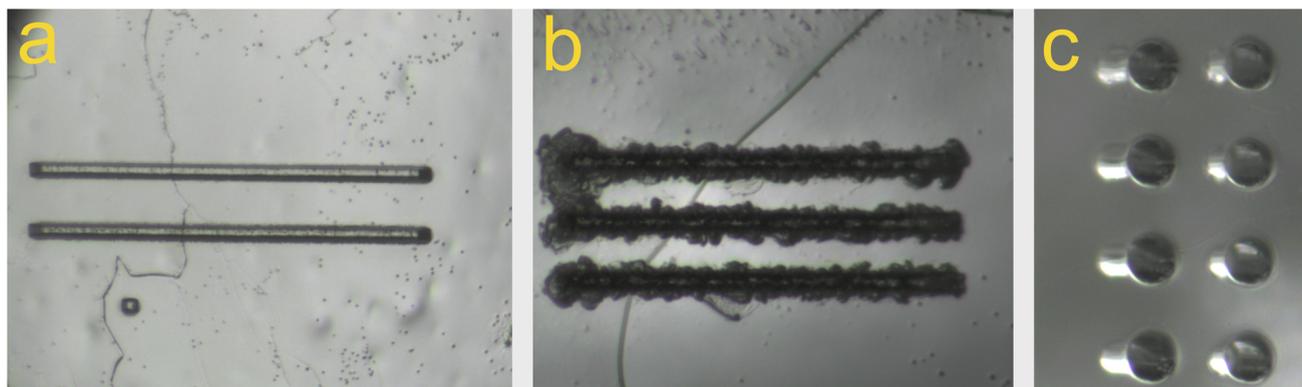

Fig. 5 Trace elemental map of a natural quartz sample for Li (top), Al (middle) and Ga (bottom) covering an area of 1.44 by 2.06 mm with a square pixel size of 48 µm. The map shows the transition from a rose-colored region of the crystal at the upper right (low Li content) to a milky region (bottom, high Li content). The high-abundance spots on the left side of the Al and Ga maps are from visible mineral inclusions in the quartz. The missing value in the Li map is an observation below the limit of detection. All abundances were calculated using Si as internal standard.

2866 | *J. Anal. At. Spectrom.*, 2025, **40**, 2857–2869

This journal is © The Royal Society of Chemistry 2025

Fig. 6 Laser camera images of line ablations in Greenland ice from the last glacial period. Each of the ablation tracks is approximately 1 cm long, crossing a clearly visible grain boundary. (a) Shows two tracks from the 157 nm laser and (b) three from the 193 nm laser, each 20 laser pulses deep. The ablation at 157 nm is generally clean and does not show any signs of destructive ablation, also when crossing the grain boundaries. At 193 nm, the ablation tracks show ragged edges and broken out fragments that are clear signs of uncontrolled ablation. (c) Shows multiple ablation craters with a 104 μm spot using the 157 nm laser for 900 (left) and 600 (right) pulses. The features of the left side of the crates are the bottom of the crates visible through the transparent ice due to the off-axis viewing of the laser camera.

wavelengths (0.33 and 0.35 J cm^{-2}) between the ablation thresholds of the other NIST SRMs at 193 nm and 157 nm. Notably different from all other investigated materials, NIST SRM614 has also higher absorption (lower penetration depth) at 157 nm than at 193 nm.

3.3 Quartz trace element map

Maps for Li, Al and Ga abundances are shown in Fig. 5, covering an area of 2.44 by 2.05 mm with a pixel size of 48 μm square. Average single-pixel LODs for the map are 0.04, 0.19 and 0.008 μg g^{-1} for Li, Al and Ga with averaged relative uncertainties of 10.9, 9.8, and 13.5% (2-σ) respectively. LODs where calculated following the approach recommended by MARLAP[45] using a variance stabilized test[46] for low background signals. Note that this test is sometimes referred to as the "Stapleton approximation" *i.e.* ref. 45 and 47.

The maps cover a transition inside a natural quartz crystal from rose-colored to milky appearance (upper right to bottom). The distribution of the trace elements reveals fine structure both at the transition zone and within the two zones as well as a number of mineral inclusions on the left side of the map. Trace element abundances vary over a few orders of magnitude with Li ranging from 0.1 μg g^{-1} to 100 μg g^{-1}, Al from 0.7 μg g^{-1} to 11 706 μg g^{-1} and Ga from 0.07 μg g^{-1} to 14 μg g^{-1}, with the highest concentrations for Al and Ga occurring in the mineral inclusions. The band of elevated Al abundances along the transition from rose to milky quartz is also visible in the optical microscopy images in Fig. 3. A geochemical interpretation of these maps is beyond the scope of this study, however, the clarity of the details resolved in the map nicely illustrates the applicability of 157 nm laser ablation for mapping of quartz and other difficult to ablate materials.

Mapping of trace elemental abundances or isotope ratios using LA-ICP-MS by continuous lateral profiling requires that the ablation takes place highly controlled and reproducible to produce maps free of artifacts. Especially in difficult-to-ablate,

poorly absorbing samples and using high on-sample fluences this requirement can pose a problem: Even if the ablation is initially controlled, once uncontrolled ablation develops, the remainder of an ablation line is usually ablated in an uncontrolled manner as well. That this is not the case here is also evident from the microscope image of the ablated area in Fig. 3.

3.4 Ablation of ice at 157 nm

At 193 nm, relatively high fluences of $\geq$5 J cm^{-2} are required to initiate ablation of natural and mQ ice at the first laser pulse. Hence, the examples shown in Fig. 6 were performed at a 193 nm fluence of 6.5 J cm^{-2}. At the shorter 157 nm wavelength much less fluence is required to initiate ablation of the ice, in fact, immediate ablation is observed at fluence below 1 J cm^{-2}. The line ablations shown in Fig. 6 are thus performed at 1.5 J cm^{-2}. Note that these fluence values were measured without the presence of ice inside the cell. Due to sublimation of the ice, there will be a small amount of water vapour present along beam path that reduces the actual on-sample fluence. This reduction however is likely negligible. Generally, at 193 nm the ablation is much less controlled than at 157 nm especially at the initial laser pulse. At 157 nm no signs of uncontrolled ablation have been observed yet, neither in the natural glacial ice shown here, nor in ice from freezing high purity water. This also holds true for ablation across grain boundaries where impurities can be highly concentrated,[48,49] which potentially alters the ablation characteristics of the ice.[29]

The relatively high fluence required at 193 nm is in line with observations by Hoffmann *et al.*,[50] who reported similar fluences for their measurements also using an Excistar laser source operated at 193 nm. Their ablation tracks also exhibit ragged edges, similar to what is shown in Fig. 6. It is noteworthy, that both earlier studies[25] as well recent ones[27,29,51] have used lower fluences (3–4 J cm^{-2}) for the ablation of ice using different ArF-laser sources with differing pulse lengths. This is

hinting at another factor controlling the ablation of ice at 193 nm than the laser wavelength alone, such as the laser pulse characteristics and/or specifics of the beam delivery system.

4 Conclusions

Here we present both design and rationale of a custom-built dual-wavelength 193 nm/157 nm cryo-LA-ICP-MS/MS system. The system is built around a modified RESOlution-SE laser ablation system and features an S155 ablation cell with a newly-developed cryo-sample holder. The LA-system uses two individual laser sources for the two wavelengths, and largely separate and individually optimized beam paths. The 193 nm system largely utilizes the normal BDU of the RESOlution-SE system (with an Excistar 193 nm laser source), whereas an entirely new beam path was custom-designed for 157 nm LA. The system can be easily reconfigured between the two wavelengths with minor hardware changes and only minor re-alignment of either beam path. This switch is also facilitated by a tight integration of the 157 nm system within the GeoStar LA software that also controls the 193 nm system. The 157 nm beam path was designed to maximize energy transmission from the laser to the sample. Even though the 157 nm BDU is not strictly a high vacuum system, the high sensitivity to contamination and the absorption of the 157 nm VUV radiation by any residual water or oxygen in the BDU necessitates that the BDU is built and treated to similar standards. In the presented system, evacuation to sub-1 hPa pressures and backfilling of the beam path with pure N_2 yields stable light transmission, even after the BDU has been vented or opened. During routine operation, the BDU is currently purged with 10 l min^{-1} of high purity N_2 with the vacuum pump running to provide an exit for the purge gas without back-diffusion and to reduce the pressure inside the BDU to around 70 hPa. In this way the overall energy transmission from the 157 nm laser onto the sample is ~54%, resulting in a workable stable maximum fluence 5 J cm^{-2}, with fluences as high as 8 J cm^{-2} achievable at smaller spot sizes. Even though these fluences are lower than what is commonly available on 193 nm systems, they have proven to be highly effective at ablating all the samples investigated here. Overall, the initial results presented here, including the 2D mapping of natural quartz, are very encouraging for the application of 157 nm laser ablation to sample matrices that are challenging to ablate at 193 nm such as quartz, sulphates, potassium salts and water ice.

Author contributions

Conceptualization of the dual-wavelength-LA-system was done by WM, AN and MS, the implementation was a collaborative effort between all the authors under the lead of AN and WM. Measurements were conceptualized by TE and WM and performed by TE, RR and MK, formal analysis and visualization was done by TE. The original draft was prepared by TE and WM, all authors contributed to the review and editing. The project was initiated by WM, who also acquired funding.

Conflicts of interest

MS and AN declare that they supplied some of the equipment used in this study in a collaborative-commercial partnership.

Data availability

Data for this article, *i.e.* crater depths and raw ICP-MS data for the 2D map, are archived on Zenodo at **https://doi.org/10.5281/zenodo.14981700**.

Acknowledgements

Notes and references

1 A. Gray, *Analyst*, 1985, **110**, 551.
2 S. Eggins, L. Kinsley and J. Shelley, *Appl. Surf. Sci.*, 1998, **127–129**, 278–286.
3 B. Fryer, S. Jackson and H. Longerich, *Can. Mineral.*, 1995, **33**, 303–312.
4 J. Gonzalez, X. Mao, J. Roy, S. Mao and R. Russo, *J. Anal. At. Spectrom.*, 2002, **17**, 1108–1113.
5 D. Günther, R. Frischknecht, C. Heinrich and H.-J. Kahlert, *J. Anal. At. Spectrom.*, 1997, **12**, 939–944.
6 D. Günther and C. Heinrich, *J. Anal. At. Spectrom.*, 1999, **14**, 1369–1374.
7 T. Jeffries, S. Jackson and H. Longerich, *J. Anal. At. Spectrom.*, 1998, **13**, 935–940.
8 S. Kelley, N. Arnaud and S. Turner, *Geochim. Cosmochim. Acta*, 1994, **58**, 3519–3525.
9 P. Sylvester and S. Jackson, *Elements*, 2016, **12**, 307–310.
10 W. Müller and J. Fietzke, *Elements*, 2016, **12**, 329–334.
11 R. Russo, X. Mao, O. Borisov and H. Liu, *J. Anal. At. Spectrom.*, 2000, **15**, 1115–1120.
12 J. Pisonero and D. Günther, *Mass Spectrom. Rev.*, 2008, **27**, 609–623.
13 J. Woodhead, J. Hergt, M. Shelley, S. Eggins and R. Kemp, *Chem. Geol.*, 2004, **209**, 121–135.
14 H. von Bergmann and U. Stamm, *Excimer Laser Technology*, Springer-Verlag, 2005, pp. 41–45.

2868 | *J. Anal. At. Spectrom.*, 2025, **40**, 2857–2869

This journal is © The Royal Society of Chemistry 2025

15 A. Bates, M. Rothschild, T. Bloomstein, T. Fedynyshyn, R. Kunz, V. Liberman and M. Switkes, *IBM J. Res. Dev.*, 2001, **45**, 605–614.

16 M. Rothschild, T. Bloomstein, J. Curtin, D. Downs, T. Fedynyshyn, D. Hardy, R. Kunz, V. Liberman, J. Sedlacek, R. Uttaro, A. Bates and C. Van Peski, *J. Vac. Sci. Technol., B:Microelectron. Nanometer Struct.–Process., Meas., Phenom.*, 1999, **17**, 3262–3266.

17 P. R. Herman, *Excimer Laser Technology*, Springer-Verlag, 2005, pp. 221–277.

18 J. Ihlemann, M. Schulz-Ruhtenberg and T. Fricke-Begemann, *J. Phys.: Conf. Ser.*, 2007, **59**, 206–209.

19 S. Dambach, *Laser-SNMS-Analysen an Aerosol-Partikeln mit Hilfe eines neu Implementierten VUV-Excimer-Lasersystems zur Einphotonenionisierung*, PhD thesis, Westfälischen Wilhelms-Universität Münster, 2009.

20 A. Pelster, M. Körsgen, T. Kurosawa, H. Morita and H. Arlinghaus, *Anal. Chem.*, 2016, **88**, 9638–9646.

21 D. Tanner, R. Henley, J. Mavrogenes and P. Holden, *Contrib. Mineral. Petrol.*, 2013, **166**, 1119–1142.

22 P. Telouk, E. Rose-Koga and F. Albarede, *Geostand. Newsl.*, 2003, **27**, 5–11.

23 S. Govorkov, K. Vogler, F. Voss and R. Pätzel, *US Pat.*, 6327290B1, 2001.

24 J. Fiebig, U. Wiechert, D. Rumble and J. Hoefs, *Geochim. Cosmochim. Acta*, 1999, **63**, 687–702.

25 W. Müller, J. Shelley and S. Rasmussen, *J. Anal. At. Spectrom.*, 2011, **26**, 2391.

26 S. Sneed, P. Mayewski, W. Sayre, M. Handley, A. Kurbatov, K. Taylor, P. Bohleber, D. Wagenbach, T. Erhardt and N. Spaulding, *J. Glaciol.*, 2015, **61**, 233–242.

27 P. Bohleber, M. Roman, M. Šala and C. Barbante, *J. Anal. At. Spectrom.*, 2020, **35**, 2204–2212.

28 S. Warren and R. Brandt, *J. Geophys. Res.: Atmos.*, 2008, **113**, D14220.

29 P. Bohleber, P. Larkman, N. Stoll, D. Clases, R. G. de Vega, M. Šala, M. Roman and C. Barbante, *Geochem., Geophys., Geosyst.*, 2024, **25**, e2023GC011425.

30 T. Bloomstein, M. Horn, M. Rothschild, R. Kunz, S. Palmacci and R. Goodman, *J. Vac. Sci. Technol., B:Microelectron. Nanometer Struct.–Process., Meas., Phenom.*, 1997, **15**, 2112–2116.

31 K. Watanabe, E. Inn and M. Zelikoff, *J. Chem. Phys.*, 1953, **21**, 1026–1030.

32 K. Watanabe and M. Zelikoff, *J. Opt. Soc. Am.*, 1953, **43**, 753.

33 E. Inn, *Spectrochim. Acta*, 1955, **7**, 65–87.

34 S. Galla, *Implementierung einer Bismut-Cluster-Primärionenquelle für Analytische Anwendungen in der Laser-Sekundärneutralteilchen-Massenspektrometrie*, PhD thesis, Westfälischen Wilhelms-Universität Münster, 2015.

35 O. Abril-Pla, V. Andreani, C. Carroll, L. Dong, C. Fonnesbeck, M. Kochurov, R. Kumar, J. Lao, C. Luhmann, O. Martin, M. Osthege, R. Vieira, T. Wiecki and R. Zinkov, *PeerJ Comput. Sci.*, 2023, **9**, e1516.

36 C. Norris, L. Danyushevsky, P. Olin and N. West, *J. Anal. At. Spectrom.*, 2021, **36**, 733–739.

37 D. Evans and W. Müller, *J. Anal. At. Spectrom.*, 2013, **28**, 1039.

38 M. Rittner and W. Müller, *Comput. Geosci.*, 2012, **42**, 152–161.

39 H. Longerich, S. Jackson and D. Günther, *J. Anal. At. Spectrom.*, 1996, **11**, 899–904.

40 K. Jochum, B. Stoll, K. Herwig, M. Willbold, A. Hofmann, M. Amini, S. Aarburg, W. Abouchami, E. Hellebrand, B. Mocek, I. Raczek, A. Stracke, O. Alard, C. Bouman, S. Becker, M. Dücking, H. Brätz, R. Klemd, D. de Bruin, D. Canil, D. Cornell, C. de Hoog, C. Dalpé, L. Danyushevsky, A. Eisenhauer, Y. Gao, J. Snow, N. Groschopf, D. Günther, C. Latkoczy, M. Guillong, E. Hauri, H. Höfer, Y. Lahaye, K. Horz, D. Jacob, S. Kasemann, A. Kent, T. Ludwig, T. Zack, P. Mason, A. Meixner, M. Rosner, K. Misawa, B. Nash, J. Pfänder, W. Premo, W. Sun, M. Tiepolo, R. Vannucci, T. Vennemann, D. Wayne and J. Woodhead, *Geochem., Geophys., Geosyst.*, 2006, **7**, 1–44.

41 K. Jochum, U. Weis, B. Stoll, D. Kuzmin, Q. Yang, I. Raczek, D. Jacob, A. Stracke, K. Birbaum, D. Frick, D. Günther and J. Enzweiler, *Geostand. Geoanal. Res.*, 2011, **35**, 397–429.

42 S. Mojtabavi, F. Wilhelms, E. Cook, S. Davies, G. Sinnl, M. Skov Jensen, D. Dahl-Jensen, A. Svensson, B. Vinther, S. Kipfstuhl, G. Jones, N. Karlsson, S. Faria, V. Gkinis, H. Kjær, T. Erhardt, S. Berben, K. Nisancioglu, I. Koldtoft and S. Rasmussen, *Clim. Past*, 2020, **16**, 2359–2380.

43 D. Della Lunga, W. Müller, S. Rasmussen, A. Svensson and P. Vallelonga, *Cryosphere*, 2017, **11**, 1297–1309.

44 P. Herman, R. Marjoribanks, A. Oettl, K. Chen, I. Konovalov and S. Ness, *Appl. Surf. Sci.*, 2000, **154–155**, 577–586.

45 MARLAP, *Detection and Quantification Capabilities*, **https://www.epa.gov/sites/default/files/2015-05/documents/402-b-04-001c-20_final.pdf**, 2004, accessed, 2025-07-14.

46 M. Huffman, *Appl. Statist.*, 1984, **33**, 224.

47 D. Strom and J. MacLellan, *Health Phys.*, 2001, **81**, 27–34.

48 D. Della Lunga, W. Müller, S. Rasmussen and A. Svensson, *J. Glaciol.*, 2014, **60**, 970–988.

49 M. Bock, J. Schmitt, L. Moller, R. Spahni, T. Blunier and H. Fischer, *Science*, 2010, **328**, 1686–1689.

50 H. Hoffmann, J. Day, R. Rhodes, M. Grieman, J. Humby, I. Rowell, C. Nehrbass-Ahles, R. Mulvaney, S. Gibson and E. Wolff, *Cryosphere*, 2024, **18**, 4993–5013.

51 P. Bohleber, K. Mervič, R. Dallmayr, C. Stremtan and M. Šala, *Talanta Open*, 2025, **11**, 100437.

This journal is © The Royal Society of Chemistry 2025

J. Anal. At. Spectrom., 2025, **40**, 2857–2869 | **2869**